

Knee-Point-Conscious Battery Aging Trajectory Prediction Based on Physics-Guided Machine Learning

Xinyu Jia, *Graduate Student Member, IEEE*, Caiping Zhang, *Senior Member, IEEE*, Yang Li, *Member, IEEE*, Changfu Zou, *Senior Member, IEEE*, Le Yi Wang, *Life Fellow, IEEE*, and Xue Cai

Abstract—Early prediction of aging trajectories of lithium-ion (Li-ion) batteries is critical for cycle life testing, quality control, and battery health management. Although data-driven machine learning (ML) approaches are well suited for this task, unfortunately, relying solely on data is exceedingly time-consuming and resource-intensive, even in accelerated aging with complex aging mechanisms. This challenge is rooted in the highly complex and time-varying degradation mechanisms of Li-ion battery cells. We propose a novel method based on physics-guided machine learning (PGML) to overcome this issue. First, electrode-level physical information is incorporated into the model training process to predict the aging trajectory’s knee point (KP). The relationship between the identified KP and the accelerated aging behavior is then explored, and an aging trajectory prediction algorithm is developed. The prior knowledge of aging mechanisms enables a transfer of valuable physical insights to yield accurate KP predictions with small data and weak correlation feature relationship. Based on a Li[NiCoMn]O₂ cell dataset, we demonstrate that only 14 cells are needed to train a PGML model for achieving a lifetime prediction error of 2.02% using the data of the first 50 cycles. In contrast, at least 100 cells are needed to reach this level of accuracy without the physical insights.

Index Terms—Accelerated aging, battery aging trajectory prediction, data-driven method, machine learning, knee point, physics-guided.

I. INTRODUCTION

WITH their high energy density and decreasing costs, lithium-ion (Li-ion) batteries have emerged as a critical form of energy storage for realizing electrified transportation and smart grids [1]. Li-ion battery cells, however, are prone to manufacturing defects and inconsistent aging behavior, leading to varying capacity fade rates and service life [2, 3]. Accurate early prediction of the aging trajectory and lifetime can be time- and cost-saving for design and quality control from a battery

This work has not been presented at a conference or submitted elsewhere previously. This work was supported in part by the National Natural Science Foundation of China under Grant 52222708 (the Excellent Young Scientists Fund), in part by the National Natural Science Foundation of China under Grant 51977007, and in part by the National Natural Science Foundation of China under Grant 52007006. (*Corresponding authors: Caiping Zhang and Yang Li*).

Xinyu Jia, Caiping Zhang, and Xue Cai are with the National Active Distribution Network Technology Research Center (NANTEC), Beijing Jiaotong University, Beijing 100044, China (email: xinyu.jia@bjtu.edu.cn; zhangcaiping@bjtu.edu.cn; 19117001@bjtu.edu.cn).

Yang Li and Changfu Zou are with the Department of Electrical Engineering, Gothenburg, 41296, Sweden (yangli@ieee.org; changfu.zou@chalmers.se).

Le Yi Wang is with the Department of Electrical and Computer Engineering, Wayne State University, Detroit 48202, USA (email:lywang@wayne.edu).

manufacturing perspective [4-6].

For aging and lifetime prediction of Li-ion batteries in normal operating conditions, data-driven methods based on machine learning (ML) techniques are considered the most convenient and practical with the recent advancements in data science and artificial intelligence [7-10]. In these conditions, battery capacity usually has no significant nonlinear relationship with the charge/discharge cycles [11]. Therefore, many well-established ML techniques have gained widespread adoption, including sample entropy and advanced sparse Bayesian predictive modeling [12], support vector machine [13], random forest [14], long short-term memory (LSTM) recurrent neural network [15], convolutional neural network (CNN) [16], and CNN-LSTM [17], amongst others. Two factors are crucial in establishing a good ML model in these works. First, health features (HFs) are manually extracted from different data curves or automatically obtained using deep learning algorithms with the help of dimensional attention mechanisms [18]. This typically requires the HFs to have a linear relationship with the prediction target to allow for good prediction accuracy. Second, it is imperative to have a significant number of training and test samples to unravel the complex battery aging patterns concealed in the data [19, 20].

Unfortunately, collecting data covering the entire battery lifetime is time-consuming since normal operating conditions necessitate an extended period to age battery cells. Therefore, high current rates and low/high temperatures are preferred to accelerate the aging process to collect the data. However, under these wider operating conditions, Li-ion cells can experience an abrupt acceleration in the aging rate before reaching their end-of-life (EOL), characterized by a *knee point* (KP) on the capacity retention curves [21, 22]. Earlier presence of the KP indicates higher system vulnerability that may cause severe safety problems if such a cell is used in practice [23, 24]. Hence, the aging prediction problem for accelerated aging batteries can be roughly simplified to model the KP reliably. In the context of accelerated aging, the task of predicting the complete behavior of Li-ion cells is challenging when only a small sample of early-life data is available. The main explanation is that the complex mechanisms during accelerated aging produce highly nonlinear and diverse patterns throughout the life cycle that may not be adequately captured in the early-age capacity data that decline linearly with cycle numbers [25]. Most existing ML-based methods attempt to find correlations

between extracted HFs and KP without considering the mechanisms behind the battery aging, partly because the mechanisms are not adequately reflected in the measurements, including current, terminal voltage, and surface temperature. In addition, similar to the challenges faced in normal operating conditions, many ML-based approaches require a vast amount of data that encompasses the entire information space for accelerated aging. These ML models need to be trained using complex deep neural networks to attain accurate predictions. However, deep learning often requires considerable computing resources, making the prediction scheme computationally inefficient and lacking cost-effectiveness [17].

Transfer learning (TL) has recently received increasing research attention in the battery community [26]. The primary purpose of TL is to use known information related to the target task in the source domain to train an ML model for the target task [27]. The method of migrating useful information from the source domain to the target task can significantly affect the performance of regression models [28]. For instance, Ma *et al.* showed that domain adaptation could improve the state of health estimation accuracy of the CNN by about 1.5% [20]. Zhu *et al.* developed a TL model to estimate battery capacity, and an extended TL model achieved a prediction error of 1.7% [29]. For the battery lifetime prediction, information can be transferred by model-based or sample-based approaches. For example, Sheng *et al.* proposed a deep CNN with ensemble learning and model-based TL for battery capacity estimation [30]. The model migration and sample selection were adopted to transfer the information from the source to the target datasets, where curve shape, long-term degradation rate, lifespan concentration, and distance between aging curves were used as criteria of curve transferability. In addition, a feature expression scoring rule based on grey relational analysis was developed to evaluate the relevance of multiple prediction tasks for battery state of health estimation [31]. In [32], early capacity sequence data of cells were used to implement pattern recognition and TL. The authors showed that unsupervised pattern analysis could help to select ML models and study useful sample knowledge.

The above works using ML and TL for battery aging prediction show that if one can select the data from the training dataset with similar information to the target task, the ML model can perform well in the target dataset. However, accurately predicting the battery lifetime for accelerated aging cells with highly nonlinear capacity fade trajectories accompanied by KPs is often daunting, especially when relying on small early-age data samples. As will be exhibited in the latter sections, the external aging characteristics show pronounced nonlinearity due to the more complex and severe internal aging mechanism of accelerated aging cells. Furthermore, since the early accelerated aging trajectory data are approximately linear, it is questionable if one can distinguish accelerated aging cells with different characteristics by simply manipulating the limited training data.

To address the challenges, this paper presents a novel physics-guided machine learning (PGML) framework that predicts the aging trajectory while taking into account the KP.

The following explains the key advantages of this proposed approach that could benefit the research community.

First, the proposed PGML framework integrates physical information and ML to predict KP. The PGML approach enhances the accuracy of training and prediction for conventional ML models when dealing with small samples and HFs having weak linear correlation. In addition, the PGML technique leverages the mechanism information to differentiate between various relationship patterns of HFs with weak linear correlation. Incorporating physical information for small battery samples has a significant impact on ML prediction performance. When physical information is unavailable, augmenting the number of training samples becomes inevitable to achieve a comparable level of ML prediction performance.

Second, a linear relationship between EOL and KP is identified. An aging trajectory prediction method considering the KP is thus proposed to select suitable time series training samples from the training dataset based on the KP prediction results and KP similarity. We validated the algorithm using two datasets of $\text{Li}[\text{NiCoMn}]O_2$ (NCM) cells and LiFePO_4 (LFP) cells. It shows that accurate KP prediction is vital for early aging trajectory prediction. If mechanism information is available, only 14 cells are needed to achieve a high prediction accuracy of 2.02% with the first 50 cycles of data (<10% of the full life-cycle data). In contrast, such a task has to be completed with at least 100 cells without using the information on degradation mechanisms.

The rest of this paper is organized as follows to detail our proposed approach. Section II describes the dataset and data preprocessing procedure, followed by Section III, which analyzes the key issues related to the early prediction of KP and aging trajectory. Section IV presents the PGML framework and the KP-conscious aging trajectory prediction method. The results of KP and aging trajectory prediction using early aging data are exhibited in Section V, where comparative analysis and discussions are also given. Finally, the main findings are summarized in Section VI.

II. DATASET AND DATA PREPROCESSING

We performed a cycle aging test for 36 NCM battery cells (denoted by Cell 1 to Cell 36) under a wide range of operating conditions. The data were collected and published in [33] for analyzing aging mechanisms and accelerated aging diagnosis. The measured data include the cell voltage, cell current, and positive and negative half-cell open-circuit voltages (OCVs) from charge/discharge cycling, hybrid pulse power characterization (HPPC) test, and low current test. 19 of the 36 cells experienced significant nonlinear accelerated aging behaviors; the rest have normal and approximately linear aging trajectories. We randomly selected 14 of the 19 cells with accelerated aging behaviors to predict their aging trajectories in terms of the capacity retention curves, EOL, and KPs. Their ambient temperatures range from 10 °C to 45 °C, and discharging current rates are between 0.5C and 2C. The corresponding aging trajectories are shown in Fig. 1(a).

It can be observed from Fig. 1(a) that the cells suffer accelerated aging after a sudden increase in the slope of the curve. We proposed an aging-speed-based method to quantify this sudden change and extract the KP [33]. First, we fit each capacity retention curve with a polynomial to characterize the capacity fade trend:

$$C_{dis}(n) = \sum_{k=0}^K a_k n^k \quad (1a)$$

where $C_{dis}(n)$ is the discharge capacity retention at the n th cycle, and a_k is the polynomial coefficient. By trial and error, the polynomial degree was selected as $K = 5$ since it can achieve high accuracy with the coefficient of determination $R^2 > 0.97$.

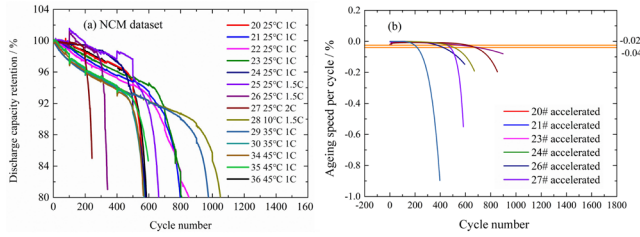


Fig. 1. Aging behaviors of 14 cells in the NCM dataset: (a) Capacity retention curves. (b) Relationship between the aging speed and the cycle number.

Next, we define the *aging speed* as

$$v = \frac{dC_{dis}(n)}{dn} < 0 \quad (1b)$$

The calculated aging speed curves for some NCM cells are plotted in Fig. 1(b). Based on the NCM dataset used in this work, we found that all the cell aging curves reduce approximately linearly before the aging speed reaches -0.025% . After that, the aging curve starts to show apparent nonlinear characteristics, and the aging will accelerate. Specifically, it takes several hundred cycles for the cell to reach the aging speed of -0.025% , whereas the aging speed will increase to -0.04% after the subsequent ten cycles, as shown in Fig. 1(b). Hence, we define the KP as the cycle number n for $v = -0.025\%$, and the calculated KPs were found to be within the 183rd to 975th cycles. The suitability of this empirical criterion for KP definition was also verified using the LFP dataset described later in Section V-E. It should be pointed out that the threshold of aging speed -0.025% can be adjusted to some extent for other aging datasets. When the KP is reached, the battery degradation rate accelerates, and the aging process intensifies at a faster pace.

With the calculated KPs, we then define the *RUL before the knee point* (*RUK*) at the n th cycle as the output to be predicted. The RUK represents the interval with normal aging and safe cycle, i.e.,

$$RUK = KP - n \quad (1c)$$

Next, 17 mechanism features (MFs), denoted by MF1 to MF17, were extracted from the evolution of the cell discharge curves, incremental capacity (IC) curves, and differential voltage (DV) curves. This feature extraction process is detailed

in Appendix. Since these MFs are highly related to the aging mechanisms, we expect some connections can be established.

III. ANALYSIS AND EXTRACTION OF DOMAIN KNOWLEDGE GUIDES

A. Analysis of Feature Relationship and Aging Characteristics of Accelerated Aging Cells

After extracting the MFs, we analyzed the feature relationships and characteristics of the 14 cells with accelerated aging. The difficulties of traditional ML methods in solving the present problem can be illustrated using Fig. 2(a), which shows the aging trajectories of four selected cells. It can be seen that Cells 21 and 24 (as well as Cells 29 and 30) have similar early linear aging trajectories but different KPs and EOLs. On the other hand, Cell 21 and Cell 30 share the same KP and EOLs, whereas their early aging trajectories differ significantly. Furthermore, Fig. 2(b) exhibits a linear relationship between KP and EOL. While the KP is a significant factor in determining the EOL, it is not reflected in the early linear trajectories. The linear relationship between KP and EOL was reported in our previous work [33]. To further illustrate this, Fig. 2(c) shows the predictive result of the early aging trajectory for Cell 21 before the presence of KP based on a conventional ML algorithm, i.e., support vector regression (SVR) with a fifth-order polynomial kernel function. Since only the first 100 cycles of capacity sequence data were used for training, the aging trajectory is approximately linear during the early aging phase. Such a technique thus fails to capture the entire aging trajectory with nonlinear patterns at later stages.

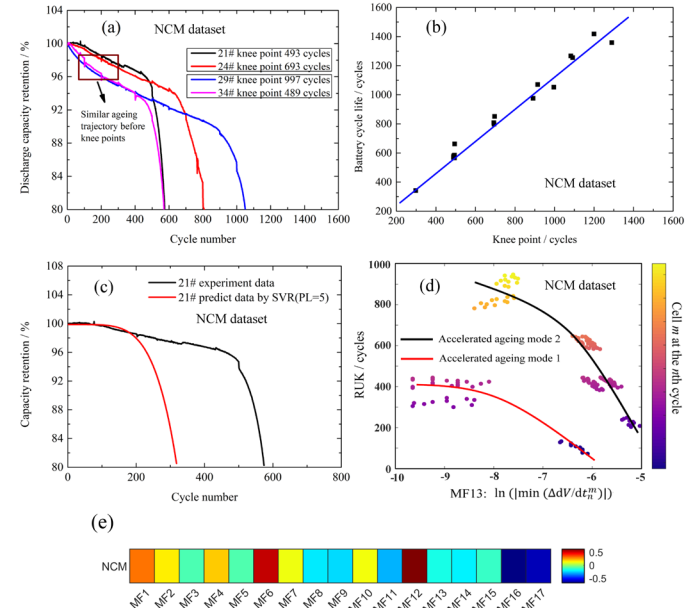


Fig. 2. Analysis of the NCM dataset: (a) Aging characteristics of accelerated aging cells. (b) Linear relationship between KP and battery life. (c) Prediction result of Cell 21's aging trajectory using SVR trained based on early linear aging data. (d) Two accelerated aging modes between MF 13 and the RUK. (e) Correlation coefficients of MFs and the RUK.

In the literature, a linear and monotonic relationship

between the MF and RUK is preferred and sometimes essential to train a good ML model [19]. For the problem at hand, we calculate the Pearson correlation coefficient r_s between the s th MF and the RUK as follows [34]:

$$r_s = \frac{\sum_{i=1}^M (MF_{s,i} - \bar{MF}_s) \cdot (RUK_{s,i} - \bar{RUK}_s)}{\sqrt{\sum_{i=1}^M (MF_{s,i} - \bar{MF}_s)^2} \cdot \sqrt{\sum_{i=1}^M (RUK_{s,i} - \bar{RUK}_s)^2}} \in [-1, 1] \quad (2)$$

where i and M are the index of the sample and the total number of samples, respectively, and the overbar represents the mean value. In Fig. 2(e), we can see that the absolute values of all the calculated r_s are less than 0.68, which is indicative of a weak correlation.

While the MFs do not display linear relationships with RUK, we notice that four mechanism features (MF11, MF13, MF14, and MF15) exhibited two distinct aging modes. For example, Fig. 2(d) shows that the relationship between the MF13 and RUK has two nonlinear patterns, represented by Mode 1 and Mode 2. For Mode 1, the corresponding RUK is smaller, so the KP with this feature relationship tends to present earlier, and the cell degrades faster. In Mode 2, the corresponding RUK is longer, indicating that the cell with this feature relationship is likely to experience later KP presence and slower degradation. Therefore, using these two aging modes indiscriminately to train an ML model will result in the underperformance of the prediction.

B. Physics Guides for Feature Relationship Pattern Recognition

The bimodal relationship between MF13 and RUK suggests that there may be specific mechanisms governing accelerated aging behaviors. Table I shows the aging modes, cell numbers, cycling temperatures, and discharge current rates for the 14 cells under investigation. According to Table I, both Mode 1 and Mode 2 can be triggered at discharge current rates of 1.5C and 1C. In contrast, Mode 1 only appears when cells are cycled at 45 °C or 10 °C. Thus, it is the temperature rather than the current rate that affects the aging mode. Unfortunately, the two aging modes cannot be separated using a single temperature value. This implies that external conditions, such as current rate and temperature, cannot serve as reliable guides for mode separation.

TABLE I.
CYCLE CONDITIONS OF 14 NCM CELLS WITH TWO MODES OF MF13

Accelerated Aging Mode	Cell Number	Cycle Temperature	Discharging Current Rate
2	20, 21, 22, 23, 24	25 °C	1C
2	25, 26	25 °C	1.5C
2	27	25 °C	2C
1	28	10 °C	1.5C
2	29, 30	35 °C	1C
1	34, 35, 36	45 °C	1C

To investigate the aging mechanisms of both modes for MF13, we conducted a non-destructive analysis based on the method proposed in our previous work [33]. We first

reconstructed the OCV versus the state of charge (SOC) curves at different cycle numbers using the positive and negative half-cell curves, measured in a 0.05-C small current test during the cycle life test [35]. With these curves, loss of positive electrode material (LAM_{PE}), loss of negative electrode material (LAM_{NE}), and loss of lithium inventory (LLI) were obtained [33]. In addition, the cell resistances (R) at different cycle numbers were also obtained via the HPPC test by dividing the voltage change by current at 1-s response time [36].

Fig. 3 displays the calculated LAM_{PE} , LAM_{NE} , LLI, and resistance related to the two modes of MF13. In, Fig. 3(a), the LLI is more pronounced in Mode 1 than in Mode 2 before the 200th cycle. Fig. 3(b) shows that the LAM_{PE} is more prominent in Mode 1 than in Mode 2 below 45°C before the 200th cycle, but not at low temperatures. Fig. 3(c) and Fig. 3(d) reveal that both the LAM_{NE} and the growth rates of internal resistance in Modes 1 and 2 are nearly indistinguishable before the 200th cycle. However, the growth rate of internal resistance is more significant at low temperatures before the 200th cycle.

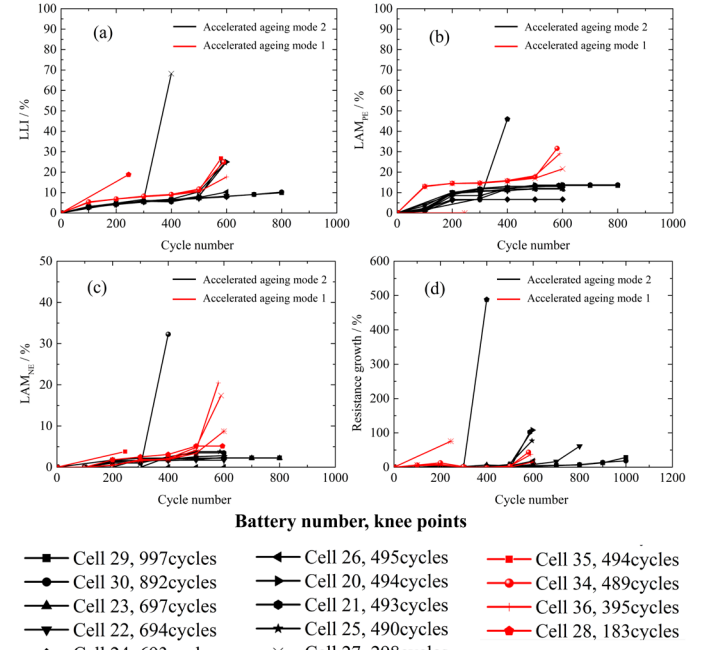


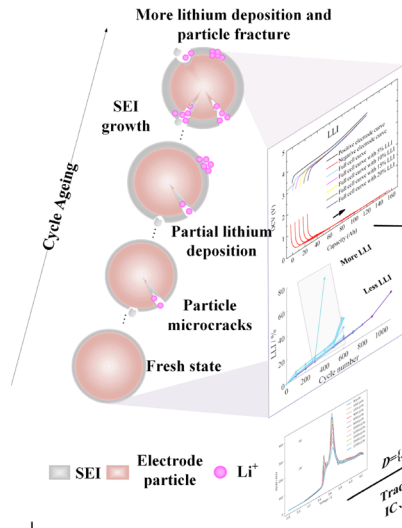
Fig. 3. Aging mechanisms of the NCM battery aging dataset. (a) LLI of two accelerated aging modes. (b) LAM_{PE} of two accelerated aging modes. (c) LAM_{NE} of two accelerated aging modes. (d) The resistance growth rate of two accelerated aging modes.

Several previous studies have investigated the impact of internal mechanisms and external conditions on LLI, LAM_{PE} , and LAM_{NE} . For example, solid electrolyte interface (SEI) growth, cathode electrolyte interphase growth [37], and lithium plating [38] are known to contribute to LLI. LAM_{PE} can be caused by various factors, such as particle cracking of positive material [39], side reactions between cathode material and electrolyte [40], and dissolution of active metal cations [41]. LAM_{NE} can arise from three main sources: chemical side reactions between graphite and electrolyte [42], particle

cracking due to Li-ion insertion and extraction [43], and co-intercalation of Li ions and other molecules into the anode [44]. Resistance growth is typically caused by SEI film growth, cathode electrolyte interphase growth, electrolyte decomposition, and current collector corrosion [45]. Furthermore, significant lithium plating and SEI growth occur on the graphite anode at low temperatures, resulting in a rapid rise in internal resistance [46]. The NCM cathode materials are relatively prone to fracture under high-temperature conditions, leading to more LAM_{PE} [47, 48]. The cathode and anode materials can experience high mechanical stress and volume changes at high discharge current rates [35]. As a result, LAM_{PE} and LAM_{NE} will be more significant at higher discharging current rates. In addition, SEI film will crack and grow rapidly due to the high temperatures caused by the high-rate discharging. Hence, the internal resistance and LLI grow faster at higher discharge current rates [49].

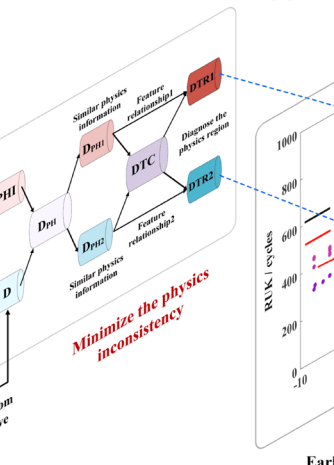
In summary, there is significant LLI, LAM_{PE}, and LAM_{NE}, as well as a rapid increase in internal resistance after the presence of the KP as a consequence of complex, interrelated mechanisms. LAM_{NE} and LAM_{PE} under the two accelerated aging modes of MF13 are indistinguishable before the KP. The distinction between the two modes is attributed to their different aging mechanisms. Specifically, Mode 1 is characterized by more severe aging mechanisms, such as the LLI and resistance growth. This suggests that aging mechanisms may be useful guides for separating the aging modes of feature relationship of each MF.

Mechanism analysis and feature engineering



Physics guided feature relationship recognition

Machine learning part



IV. METHODOLOGY

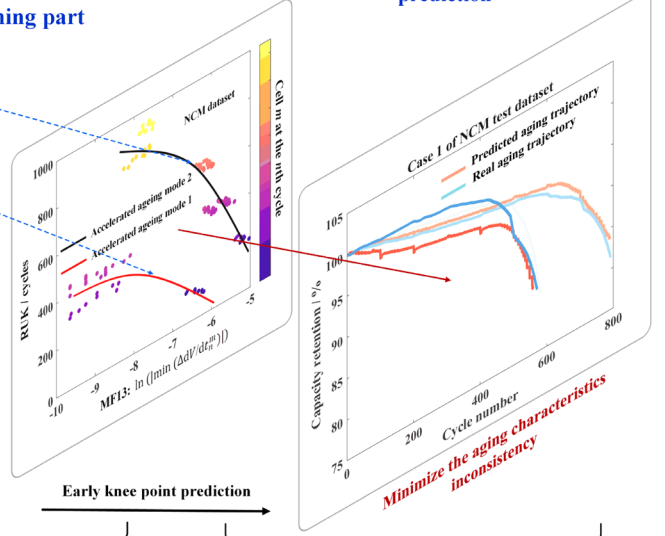
A. PGML and Knee-Point-Conscious Aging Trajectory Prediction

As demonstrated in the previous section, we discovered a close correlation between the feature relationship MF13 and aging mechanisms, which can be distinguished as Modes 1 and 2 by identifying LLI, LAM, or resistance growth. The two modes in MF13 versus RUK relationship can be viewed as two regression routes, where physical information is used to help ML algorithms select the more suitable route. We thus regard the combination of physics guide and ML as *physics-guided machine learning*. We leverage these relationships to develop PGML for aging trajectory prediction that takes into account KP in this section. The PGML, as shown in Fig. 4, consists of two main steps:

- 1) Analyzing aging mechanisms by reconstructing OCV curve to obtain physical information and extracting mechanism features from discharge curves, IC curves, and DV curves;
- 2) Employing physics-guided feature relationship recognition to minimize physical inconsistency and enhance the prediction performance of ML models on small datasets.

After obtaining KPs with PGML, the next step is to predict the aging trajectories using an accelerated aging characteristics minimization approach. To achieve this, KP similarity is used to select time-series samples for training the ML model considering the linear relationship between KP and cycle life. The algorithmic details are provided in the subsequent subsections.

Early knee point and aging trajectory prediction



Physics guided machine learning

Knee point conscious ageing trajectory prediction

Fig. 4. Framework of the PGML and knee point conscious aging trajectory prediction.

B. Decision Tree Regression and Classification Models

Decision tree regression (DTR) is chosen for KP prediction due to its shorter training time, higher accuracy, and better

robustness than many state-of-the-art ML methods [50]. The DTR builds an “if-then” tree structure to predict the output values. It generally involves the following steps.

Step 1: Data preparation. Denote $X = [X_1, X_2, \dots, X_j, \dots, X_J]$ as the input matrix and $Y = [RUK_1, RUK_2, \dots, RUK_m, \dots, RUK_M]^T$ as the RUK label vector of the aging cell. Here, $X_j = [x_{1,j}, x_{2,j}, \dots, x_{m,j}, \dots, x_{M,j}]^T$ is an M -dimensional feature vector for the j th feature, J is the total number of features, and M is the total number of samples in each feature vector. In the input space X , where the training dataset is located, we recursively divide a region into two subregions and determine the output values. A split node is selected when a specific region or subregion is divided.

Step 2: Select the optimal splitting feature j and cleavage h , and two regions can be obtained, denoted as $R_1(j, h) = \{x_{m,j} | x_{m,j} \leq h\}$ and $R_2(j, h) = \{x_{m,j} | x_{m,j} > h\}$. Find the optimal j and h by solving the following optimization problem:

$$\min_{j,h} [\sum_{x_{m,j} \in R_1} (RUK_m - c_1)^2 + \sum_{x_{m,j} \in R_2} (RUK_m - c_2)^2] \quad (3)$$

$$c_1 = \frac{1}{N_1} \sum_{x_{m,j} \in R_1(j,h)} RUK_m \quad (4)$$

$$c_2 = \frac{1}{N_2} \sum_{x_{m,j} \in R_2(j,h)} RUK_m \quad (5)$$

where c_1 and c_2 are the total output values for the two subregions, and N_1 and N_2 are the numbers of samples in R_1 and R_2 , respectively.

Step 3: Repeat Step 2 on both subspaces until the termination condition is met.

Step 4: Divide the dataset $D = [X, Y]$ into P subregions R_1, R_2, \dots, R_P , and the final generated DTR is:

$$RUK = DTR(X) = \sum_{p=1}^P c_p I_p \quad (x_{m,j} \in R_p) \quad (6)$$

$$I_p = \begin{cases} 1, & \text{if } (x_{m,j} \in R_p) \\ 0, & \text{if } (x_{m,j} \notin R_p) \end{cases} \quad (7)$$

$$KP = RUK + n \quad (8)$$

where c_p is the output value for the p th subregion.

A decision tree classification (DTC) model is built to diagnose the type of feature relationship (accelerating aging mode) of the target cells. The steps to build the DTC model are similar to those of the DTR model above [51]. The main difference is that the DTC model is designed to learn the mapping between the feature vectors and the relationship classification labels, thereby enabling it to classify data points based on their intrinsic relationships accurately.

C. Performance Evaluation Indices

The indices used to evaluate the performance of our method include the root mean square error (RMSE) that measures the difference between a series of predicted and the true values under a given condition, the mean absolute error (MAE), and the mean absolute percentage error (MAPE) that assess the prediction accuracy of the model under all conditions and the mean RMSE (MRMSE) that measures the difference between the predicted and true actual values under all conditions, i.e.,

$$RMSE_k = \sqrt{\frac{1}{Z} \sum_{i=1}^Z (\hat{y}_{i,k} - y_{i,k})^2} \quad (9)$$

$$MAE = \frac{1}{Z} \sum_{i=1}^Z |\hat{y}_i - y_i| \quad (10)$$

$$MAPE = \frac{1}{Z} \sum_{i=1}^Z \frac{|\hat{y}_i - y_i|}{y_i} \times 100\% \quad (11)$$

$$MRMSE = \frac{1}{N} \sum_{k=1}^N RMSE_k \quad (12)$$

where y and \hat{y} represent the true and predicted outputs, respectively, i is the index of samples, Z is the total number of samples, k is the index of conditions, and N is the total number of conditions. In addition, accuracy (ACC) is used to evaluate the performance of ML classification models, defined as

$$ACC = \frac{TP+TN}{TP+TN+FP+FN} \times 100\% \quad (13)$$

where TP is the number of the positive samples diagnosed as positive samples, TN is the number of the negative samples diagnosed as negative samples, FP is the number of positive samples diagnosed as negative samples, and FN is the number of negative samples diagnosed as positive samples.

D. A Physics-Guided Machine Learning Method

This subsection outlines the development of the PGML architecture tailored for small datasets that incorporate physical information. We present in Fig. 5 a schematic representation of the PGML, which comprises three distinct components as detailed below.

1) Feature Extraction and Physical Information Acquisition

We aim to reduce the physical differences between the training and the test data in this mechanism-driven part. First, as in the conventional ML algorithms, we can obtain a training data matrix $D = [X, Y]$ based on conventional measurements, where X and Y are defined earlier in Section IV-B. The MFs, LLI, LAM_{PE}, LAM_{NE}, and resistance of each cell are calculated based on the methods in Sections II and III.

2) Physics-Guided Feature Relationship Separation

Next, we use the physical information to form a physics-enhanced data matrix $D_{PH} = [X_{PH}, Y]$ where $X_{PH} = [X_1, X_2, \dots, X_j, \dots, X_J, X_{LLI}, X_{LAMPE}, X_{LAMNE}, X_R]$ is the new input data matrix. Here, X_{LLI} , X_{LAMPE} , X_{LAMNE} , and X_R are four physical feature vectors containing LLI, LAM_{PE}, LAM_{NE}, and resistance information, as described in Section III-B. To optimize the prediction accuracy, our next step involves identifying an appropriate *mechanistic segmentation point*, chosen from X_{LLI} , X_{LAMPE} , X_{LAMNE} , and X_R , which will enable us to divide D_{PH} into two sub-matrices. This can be done by repeatedly selecting a candidate segmentation point from X_{LLI} , X_{LAMPE} , X_{LAMNE} , or X_R . For example, when an element $x_{seg,LLI}$ in X_{LLI} is selected, D_{PH} can be divided into two sub-matrices, e.g.,

- a) $D_{PH1} = [X_{PH1}, Y_1]$, where $x_{min,LLI} < x_{seg,LLI} < x_{m,LLI} < x_{max,LLI}$
- b) $D_{PH2} = [X_{PH2}, Y_2]$, where $x_{min,LLI} < x_{m,LLI} < x_{seg,LLI} < x_{max,LLI}$

where $x_{\min,LLI}$ and $x_{\max,LLI}$ are the minimum and maximum elements in X_{LLI} , respectively. Based on D_{PH1} and D_{PH2} , two ML regression models are trained for each MF, and we identify the MF with the minimum RUK prediction error as the best MF for the selected $x_{seg,LLI}$. By conducting an exhaustive search of all elements in X_{LLI} , $x_{m,LLI}$ with the highest prediction accuracy is used as the candidate segmentation point for LLI, and the corresponding best MF and accuracy are recorded. The above procedure is repeated for X_{LAMPE} , X_{LAMNE} , and X_R , and the final mechanistic segmentation point and MF corresponds to the best MF with the minimum prediction error. The corresponding division is denoted by $D_{relationship,PH1} = [X_{v,1}, RUK_1]$, $D_{relationship,PH2} = [X_{v,2}, RUK_2]$, where v is the index of the best MF.

3) Binary Machine Learning Training and Prediction

Finally, we adopt $D_{relationship,PH1}$ and $D_{relationship,PH2}$ to train two DTR models $f_{PH1}: X_{v,1} \rightarrow RUK_1$ and $f_{PH2}: X_{v,2} \rightarrow RUK_2$, respectively. We then obtain $D_{diagnosis} = [X_{diagnosis}, Y_{diagnosis}]$, where $X_{diagnosis} = [X_{PH1dia}, X_{PH2dia}]^T$ and $Y_{diagnosis} = [Y_{diagnosis1}, Y_{diagnosis2}]^T$. The feature vectors in $X_{diagnosis}$ include 17 MFs without mechanism information. Here, $Y_{diagnosis1}$ is 0 for the feature vector X_{PH1dia} , and $Y_{diagnosis2}$ is 1 for the feature vector X_{PH2dia} . We train an ML classification model f_{MLC} (the DTC) to determine which DTR model (f_{PH1} or f_{PH2}) the target battery feature vector $X_{v,target}$ belongs to, i.e., $f_{MLC}: X_{diagnosis} \rightarrow Y_{diagnosis}$. The feasibility of diagnosing two feature relationship patterns under different physics regions is shown in our previous work [33]. We use the selected DTR model to predict the KP of the target cell with its feature vector $X_{v,target}$.

According to the analysis in Section III-A, there is a linear relationship between the KP and cycle life. Therefore, we train an SVR model with a linear kernel function to learn the relationship between KP and cycle life on the source dataset. Finally, we feed the predicted KP to the SVR model to predict the cycle life of the target cells.



D: traditional feature matrix. D_{PH} : physics enhanced feature matrix. PHI: physics information.
 D_{PH1} and D_{PH2} : physics enhanced feature submatrix from separating D with physics information.
 f_{MLC} : classification machine learning model.
 f_{PH1} : machine learning regression model with physics enhanced feature submatrix1.
 f_{PH2} : machine learning regression model with physics enhanced feature submatrix2.

Fig. 5. Schematics of PGML.

E. Knee-Point-Conscious Aging Trajectory Prediction

Given the strong correlation between the aging trajectory and KP, we developed a method for predicting the aging

trajectory based on KP similarity. First, we select the transferable time series sample from the source dataset according to KP similarity. The KP similarity is measured by the distance d :

$$d = |KP_{pre} - KP_{true}| \quad (14)$$

where KP_{pre} and KP_{true} represent the predicted and the true KPs, respectively. By doing so, inconsistent characteristics of accelerated aging cells are minimized. Then, we train a DTR model with the selected transferable time series sample. Finally, we use the trained DTR model to predict the aging trajectory of target cells. We denote the method PGML-DTR in the rest of the work.

V. RESULTS AND DISCUSSION

A. Early Knee Point Prediction Results Based on NCM Dataset

The NCM dataset was divided into four cases to validate the proposed KP-conscious aging trajectory prediction algorithm. For each case, three cells were chosen for testing, and the rest were used for model training, as shown in Table II. MFs were extracted every five cycles between the 50th cycle and the 90th cycle.

The PGML-DTR uses a full-cell OCV-SOC reconstruction method to obtain each cell's LLI, LAM_{PE}, and LAM_{NE}, and the resistance of each cell was obtained from the HPPC test. Then, we used the physical information to find the separable feature relationship for each feature. The relationship between each MF and KP can be separated into two sub-relationships according to the difference in aging mechanisms. For the four cases, the best feature relationship is MF15, determined by the PGML, and its best physics separation point is determined according to LLI.

TABLE II.
TRAINING AND TEST CELLS FOR THE 4-FOLD VALIDATION ON THE NCM DATASET

Case	Training cells	Test cells
Case 1	21,23,24,26,27,28,29,30,34,35,36	20,22,25
Case 2	20,22,24,25,27,28,29,30,34,35,36	21,23,26
Case 3	20,21,23,24,25,27,28,29,30,35,36	22,26,34
Case 4	20,21,22,24,26,27,28,29,30,35,36	23,25,34

The two feature relationship patterns can be classified with ACC = 100% based on the proposed DTC model. After the feature relationship separation, we trained two DTR models with two relationships between MF15 and RUK for KP prediction. The KP prediction results are summarized in Table III, where it can be seen that the average MAPE of four cases is 4.05% with the aging data of the 50th cycle on the training datasets. The corresponding average MAPE of four cases is 4.18%, the average MAE is 22.44 cycles, and the average MAE of four cases is 22.58 cycles. The results show that the proposed PGML-DTR can accurately predict the KP with only 11 cells for training when the physical information is combined with ML. Fig. 6 depicts the KP prediction outcomes achieved via the PGML-DTR method, with an MAE of approximately 25 cycles

and an MAPE ranging from 0.76% to 7.4%. Therefore, the proposed PGML-DTR can effectively predict the KP with very few cells and early aging data under complex cycle conditions.

B. Early Aging Trajectory and Life Prediction Results Based on NCM Dataset

We train an SVR model with a linear kernel using the linear relationship between the KP and cycle life. The KPs of the target cells are predicted by the PGML. Then, the predicted KPs are fed into the SVR model for cycle life prediction. The EOL prediction results are shown in Table IV, Fig. 7, and Fig. 8.

The MAE and MAPE are used to evaluate the EOL prediction accuracy. The RMSE and MRMSE are used to evaluate the aging trajectory prediction accuracy. According to Table IV and Fig. 7, the early aging trajectory prediction error is 2.02% with the 50th cycle of data in the NCM dataset. According to Table IV and Fig. 7, the aging trajectory prediction of four cases can be accurately predicted with an EOL prediction error of 8.47%. In Fig. 8, the aging trajectory prediction error is all less than 3% for all four NCM cases. In Fig. 7, though the accuracy of the aging trajectory prediction is very high, the apparent errors existed in the mid-stage of the capacity degradation curve. The mid-stage of the capacity degradation curve before the knee point is approximately linear. In this paper, the knee point-conscious aging trajectory prediction method mainly considers the knee point influence. The knee point conscious aging trajectory prediction method predicts the entire nonlinear aging trajectory well with early linear capacity sequence data. Therefore, the knee point conscious aging trajectory prediction method has some errors during the linear stage before the knee point, and can predict the aging trajectory accurately after the knee point.

TABLE III.

MAPE AND MAE RESULTS OF KP PREDICTION FOR THE FOUR CASES NCM CELLS DATASETS WITH PGML-DTR AT THE 50TH CYCLE

Case	Training dataset		Test dataset	
	MAE / cycles	MAPE / %	MAE / cycles	MAPE / %
Case 1	21.61	3.87	21.37	3.68
Case 2	22.52	4.06	21.5	4.2
Case 3	22.71	4.13	29.16	5.29
Case 4	22.93	4.17	18.29	3.57
Average	22.44	4.05	22.58	4.18

TABLE IV.

EARLY LIFE PREDICTION RESULTS WITH THE 50TH CYCLE DATA ON THE NCM DATASET

Case	MAE / cycles	MAPE / %	MRMSE / %
Case 1	35.5	5.04	1.95
Case 2	80.16	11.63	2.84
Case 3	65.23	9.84	2.06
Case 4	54.75	7.4	1.23
Average	58.91	8.47	2.02

C. Enable Machine Learning to Study and Understand the Insightful Physics Knowledge

To further study the influence of the physical mechanism on the feature relationship of Li-ion batteries, we classified the 17

feature relationships of 14 NCM cells according to the LLI, LAM, and resistance of the cells before the 90th cycle. According to Fig. 9(a), the MAPE of the DTR training can be significantly reduced by the PGML. As shown in Fig. 9(b), each feature relationship has a most suitable mechanistic separation point. Each feature relationship can be separated into two sub-relationships with similar physics information. The MAPE of the DTR model with each feature relationship can decrease by about 5.23%–13.83%. Compared to conventional ML methods, PGML yields an impressive 50% improvement in DTR prediction accuracy when the single weak correlation feature relationship is used to train the DTR model. Our work thus shows the potential of using physical information to enhance the identification of the feature relationship patterns of Li-ion batteries.

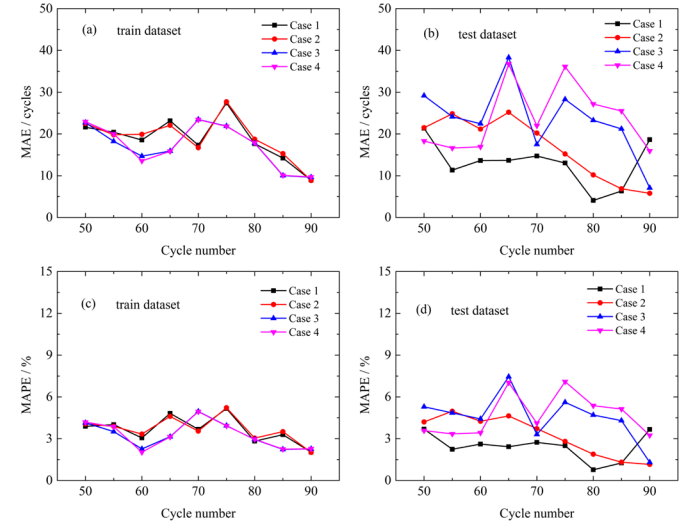


Fig. 6. KP prediction results: MAE and MAPE from the 50th cycle to the 90th cycle of four cases on the NCM dataset with PGML-DTR. (a) MAE of KP prediction on the training dataset. (b) MAE of KP prediction on the test dataset. (c) MAPE of KP prediction on the training dataset. (d) MAPE of KP prediction on the test dataset.

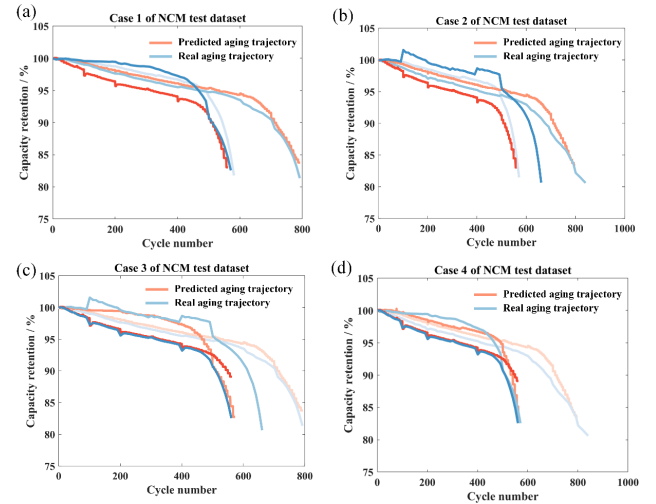


Fig. 7. Aging trajectory prediction results of 4 cases on the NCM test dataset by KP-conscious aging trajectory prediction method with the 50th cycle data. (a) Case 1. (b) Case 2. (c) Case 3. (d) Case 4.

D. Comparison Analysis for the Early Knee Point Prediction with PGML

1) Early knee point prediction with different machine learning methods

Based on the results of Section V-A, it can be seen that PGML-DTR can accurately predict KP. In addition to DTR, other ML methods, such as k-nearest neighbor regression (KNN), random forest regression (RFR), artificial neural networks (ANN), and SVR, also have excellent regression and prediction capabilities. This subsection compares the KP prediction results of PGML combined with other conventional ML algorithms with the same feature and mechanism information. Table V shows that the KP prediction accuracy of PGML-DTR at the 50th cycle is higher than PGML-KNN, PGML-RFR, PGML-ANN, and PGML-SVR. Except for the KP prediction error of PGML-SVR, which is 16.2%, the prediction error of other ML methods under the PGML framework is less than 9%.

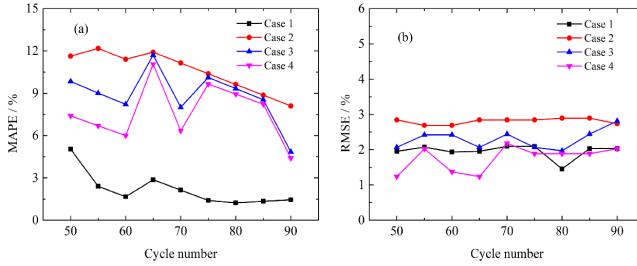


Fig. 8. Early EOL and aging trajectory results from the 50th cycle to the 90th cycle of four cases on the NCM dataset with the KP-conscious aging trajectory method. (a) EOL results. (b) Aging trajectory results.

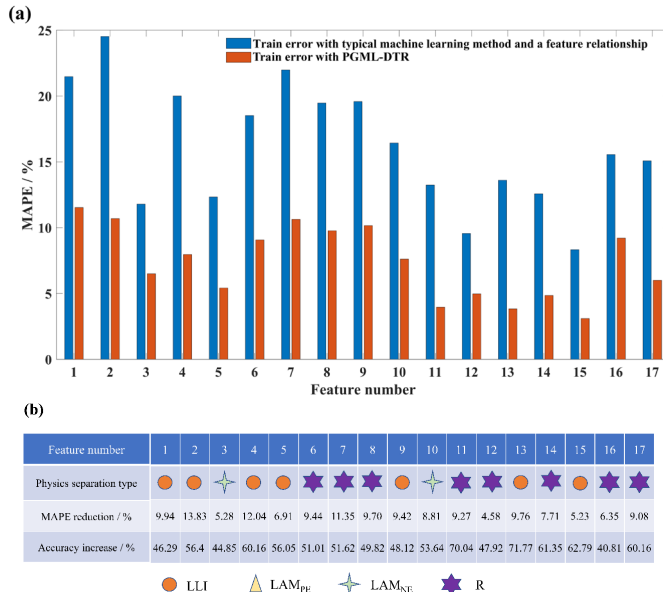


Fig. 9. Feature relationship separation results of NCM cells. (a) Training results of the DTR model with a conventional ML method and PGML-DTR. (b) Physics separation type for the 17 feature relationships of NCM cells.

As shown in Fig. 10, the KP prediction accuracy of PGML-DTR and PGML-KNN is high, and the predicted MAPEs on the

test dataset are all about 5%. On the contrary, the KP prediction errors of PGML-SVR are large, and the predicted MAPE of PGML-SVR on the four test datasets are all higher than 10%. The predicted MAPE of PGML-ANN on test dataset 2 is less than 5%, but the predicted MAPEs of PGML-ANN on test datasets 1, 3, and 4 are greater than 10%. Compared with the PGML-DTR, the PGML-RFR has a worse KP prediction accuracy on four cases of NCM battery datasets.

Based on the above comparison, we can conclude that 1) the PGML can adapt to different ML models and ensure high KP prediction accuracy on small sample datasets with physical information. 2) DTR is more suitable for PGML than other investigated ML algorithms.

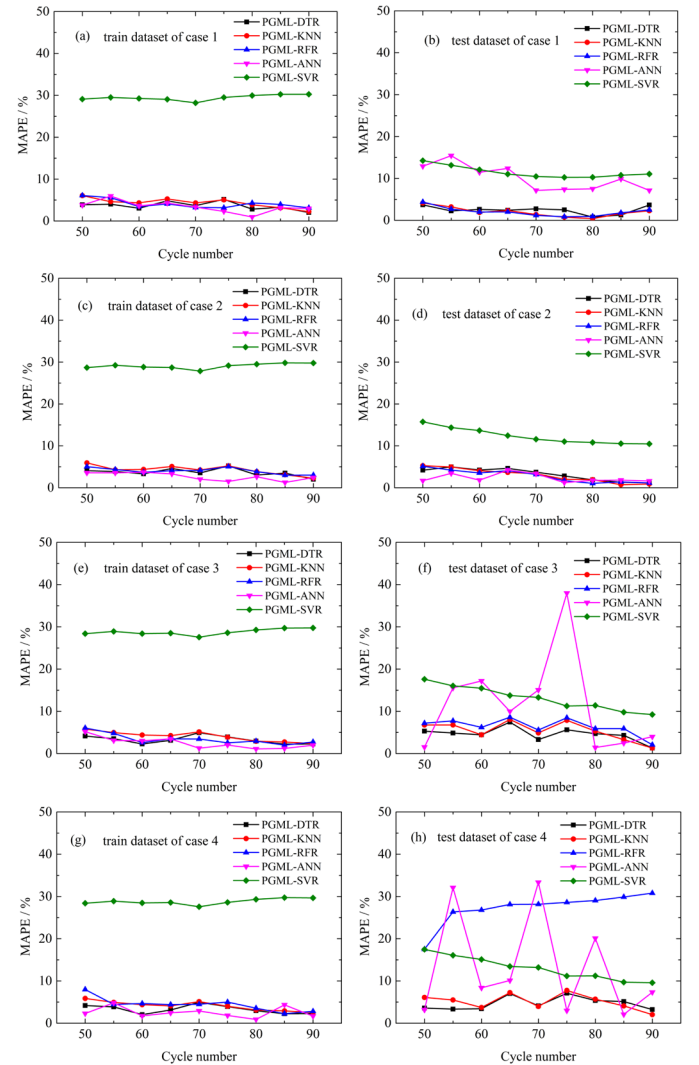


Fig. 10. MAPE of KP prediction from the 50th to the 90th cycles of four cases on the NCM dataset with PGML and different ML models. (a) Training dataset of Case 1. (b) Test dataset of Case 1. (c) Training dataset of Case 2. (d) Test dataset of Case 2. (e) Training dataset of Case 3. (f) Test dataset of Case 3. (g) Training dataset of Case 4. (h) Test dataset of Case 4.

2) Comparison analysis for the early knee point prediction with conventional machine learning methods

Next, we compare the KP prediction accuracy of PGML-

DTR and some traditional ML algorithms. As shown in Fig. 11, traditional ML architectures often do not consider physical information. When a feature exhibits a strong correlation with KP, it will be selected as an input of the ML model. Since the features on the NCM dataset do not correlate strongly with KP, all 17 features are used as the input of the traditional ML models.

As shown in Table VI, at the 50th cycle, PGML-DTR has higher KP prediction accuracy than DTR, RFR, KNN, ANN, and SVR. The KP prediction error of PGML-DTR is 4.18%, whereas the predicted MAPE of conventional ML algorithms are all greater than 9%. As shown in Fig. 12, from the 50th to the 90th cycles, the KP prediction accuracy of PGML-DTR is higher than the conventional ML algorithms. The predicted MAPEs of PGML-DTR are all within 5%. The KP prediction errors of the conventional ML algorithms are large, with predicted MAPE greater than 10% on all four test datasets. We can see that for small sample datasets with physical information, PGML-DTR has better KP prediction capability than DTR, RFR, KNN, ANN, and SVR, especially when the features do not correlate strongly with the prediction target.

TABLE V.

KP PREDICTION MAPE FOR THE FOUR CASES OF NCM TEST DATASETS BY PGML WITH DIFFERENT ML METHODS AT THE 50TH CYCLE

	PGML-DTR	PGML-KNN	PGML-RFR	PGML-ANN	PGML-SVR
Case 1	3.68%	4.12%	4.37%	12.8%	14.2%
Case 2	4.2%	5.26%	5.12%	1.67%	15.7%
Case 3	5.29%	6.75%	7.71%	1.52%	17.5%
Case 4	3.57%	6.1%	17.5%	3.17%	17.4%
Average	4.18%	5.56%	8.69%	4.79%	16.2%

TABLE VI.

KP PREDICTION MAPE FOR THE FOUR CASES OF NCM TEST DATASETS BY CONVENTIONAL ML METHODS AND PGML-DTR AT THE 50TH CYCLE

	PGML-DTR	DTR	KNN	RFR	ANN	SVR
Case 1	3.68%	14.2%	22.5%	6.09%	12.4%	295%
Case 2	4.2%	3.54%	10.9%	10.1%	29.1%	58.9%
Case 3	5.29%	11.5%	12.3%	9.51%	16.8%	249%
Case 4	3.57%	11.4%	8.38%	14.1%	19.7%	29.2%
Average	4.18%	10.2%	13.5%	9.95%	19.5%	158%

E. Impact of the Amount of Cell Sample on KP Prediction Accuracy of DTR Without Physics Information

In the previous subsection, we show the effectiveness of PGML-DTR for KP prediction on a small sample dataset with mechanism information. This subsection focuses on the effect of the number of training samples on the KP prediction accuracy of the DTR model for Li-ion batteries. Since the NCM dataset has limited samples, for this purpose, we adopted an LFP dataset containing 123 accelerated aging LFP cells [19]. Fig. 13(a) shows the aging trajectories of the 123 LFP cells. The decline curves of the LFP cells are all nonlinear with KPs. As shown in Fig. 13(b), similar to the NCM cells, the KP and EOL of the LFP cells also have a strong linear relationship, where the correlation coefficient is 0.9952. Fig. 13(c) shows the correlation between the 17 mechanism features used in this paper and the KP of the LFP cells. It can be seen that there is no

strong linear correlation between the 17 mechanism features and KP.

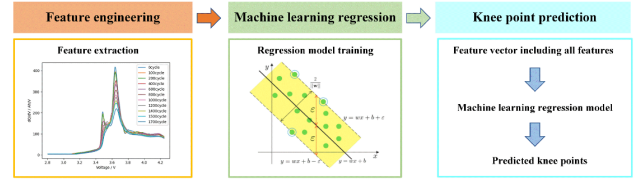


Fig. 11. Conventional ML framework for KP prediction.

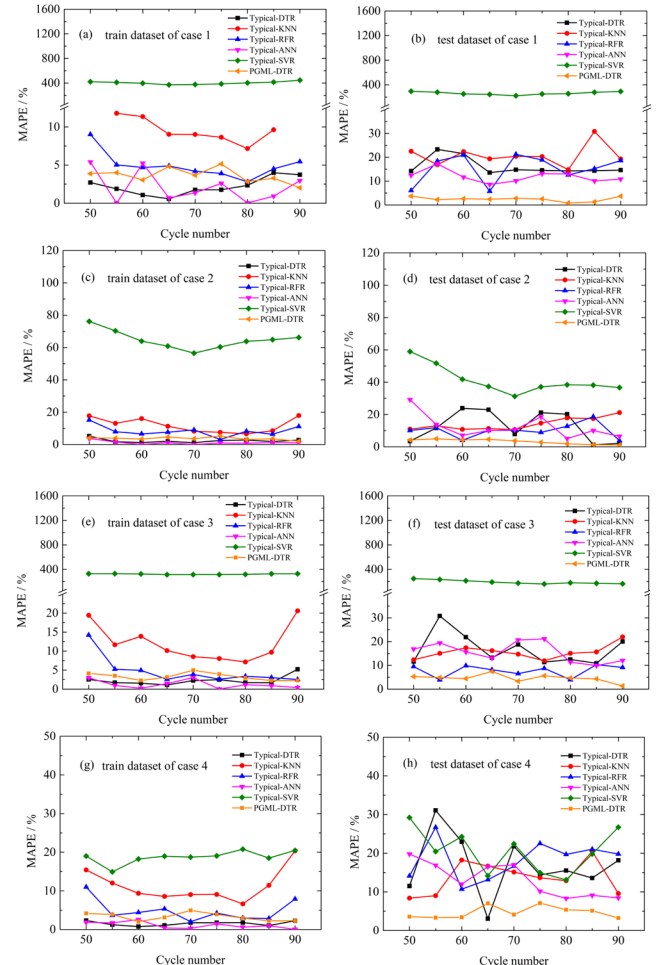


Fig. 12. MAPE of KP prediction from the 50th to the 90th cycles on the NCM dataset with PGML-DTR and conventional ML frameworks. (a) Training dataset of Case 1. (b) Test dataset of Case 1. (c) Training dataset of Case 2. (d) Test dataset of Case 2. (e) Training dataset of Case 3. (f) Test dataset of Case 3. (g) Training dataset of Case 4. (h) Test dataset of Case 4.

Since the LFP dataset does not provide mechanistic information, the PGML architecture cannot be used. Fortunately, since the sample size of the LFP dataset is nearly ten times larger than that of the NCM, we can use the traditional ML methods to investigate the effect of the number of training samples on the KP prediction accuracy of the DTR model. 23 of the 123 LFP cells were randomly selected as the test set, and the rest were used for training with different training sample sizes and cycle numbers of feature extraction. Finally, a total of

10,000 training and test datasets are randomly generated.

As shown in Fig. 14, the MAPE of KP on the training and test datasets decreases with increased training samples. When the number of cells used for training is less than 40, the predicted MAPE of KP on the test dataset will be greater than 50%. The MAPE of training and testing decreases when the number of cells for training is between 40 to 100. However, the cycle number used for feature extraction has no significant effect on the KP prediction MAPE of the DTR model. Therefore, for the DTR model, increasing the number of training samples is an effective way to improve the accuracy of the DTR model in the absence of physical information. In summary, in KP prediction, small samples can be used for PGML-DTR by providing additional physical information regarding aging mechanisms. When physical information is unavailable, traditional ML algorithms must increase the number of training samples.

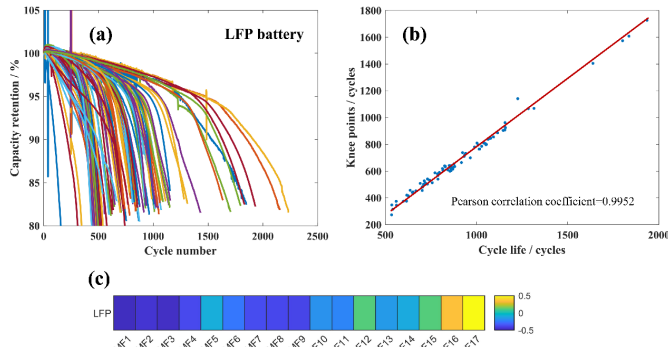


Fig. 13. Aging characteristics and feature correlation analysis of LFP cells. (a) Accelerated aging curves of LFP cells. (b) Linear interdependency between KP and battery life. (c) Correlation coefficients of MFs and the RUK for LFP cells.

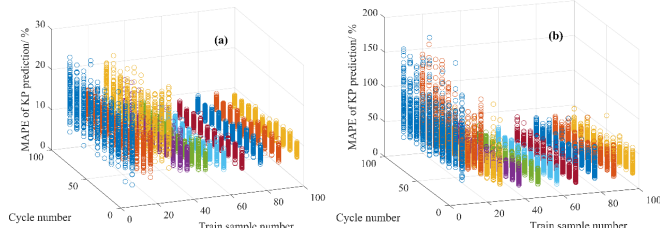


Fig. 14. KP prediction results with DTR and different train sample numbers on the LFP dataset: (a) Training dataset. (b) Test dataset.

F. Validating Prediction Accuracy and Generalization of Knee Point Conscious Aging Trajectory Prediction on the LFP Cell Dataset

The LFP cell dataset was used to validate the KP-conscious aging trajectory prediction accuracy based on the training and test data sets of four LFP cells from the 10,000 data sets generated in Section V-E. The training dataset contains 100 cell samples and features of the fifth cycle. The KP prediction results are shown in Table VII, which shows that the MAPE of DTR is 9.6%.

The prediction results of EOL and aging trajectory are shown in Table VIII and Fig. 15, respectively. The EOL prediction error is 7.48% with the data of five cycles, and the

aging trajectory prediction error is 2.68%. The results indicate that the proposed algorithm is not only applicable to NCM cells but also highly effective for LFP cells. This is owing to the strong correlation between the aging characteristics and KP of both NCM and LFP cells, leading to the high adaptability and accuracy of the algorithm. The high accuracy of the aging trajectory and lifetime prediction is mainly attributed to the accurate prediction of KP.

TABLE VII.
EARLY KP PREDICTION RESULTS FOR THE FOUR CASES OF LFP DATASETS BY DTR WITH THE FIFTH CYCLE DATA

Case	Training dataset		Test dataset	
	MAE/cycles	MAPE / %	MAE / cycles	MAPE / %
Case 1	47.1	8.34	51.1	9.44
Case 2	51.5	8.93	75.4	9.83
Case 3	51.7	9.38	49	9.62
Case 4	49.9	9.17	55.6	9.54
Average	50.05	8.95	57.7	9.60

TABLE VIII.
EARLY LIFE PREDICTION RESULTS WITH THE FIFTH CYCLE DATA IN THE LFP TEST DATASET

Case number	MAE / cycles	MAPE / %	MRMSE / %
Case 1	52.88	6.87	2.91
Case 2	83.15	8.51	2.11
Case 3	54.27	7.49	2.78
Case 4	56.72	7.06	2.94
Average	61.75	7.48	2.68

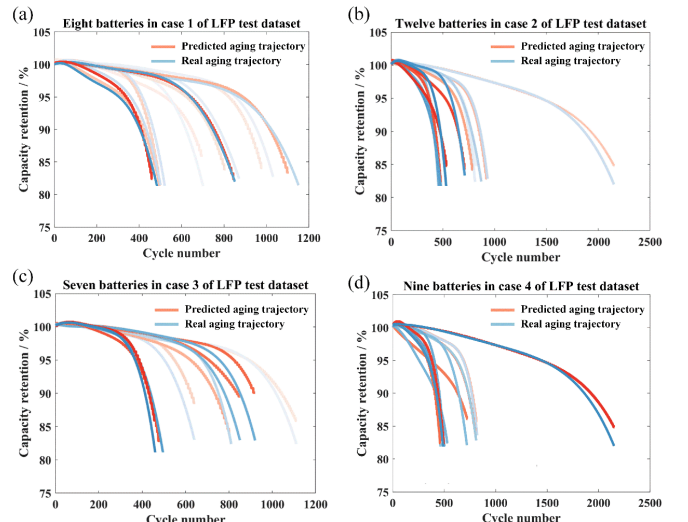


Fig. 15. Aging trajectory prediction results of four cases on the LFP test dataset by KP-conscious aging trajectory prediction method with the fifth cycle data. (a) Case 1. (b) Case 2. (c) Case 3. (d) Case 4.

VI. CONCLUSION

ML is a promising technique for Li-ion battery health management and prognostics. However, for early prediction of accelerated aging cells, complex aging mechanisms and unfavorable operating conditions will reduce the accuracy of ML in the life prediction of Li-ion batteries. We developed a PGML-DTR framework that combines a physics guide and DTR for the KP-conscious aging trajectory prediction with early-age data. Using the PGML-DTR, the KP prediction error

is less than 4.2% on an NCM dataset with small training battery samples. With the DTR, the KP prediction error is 9.6% on an LFP dataset when we have a large sample size for training. We then obtained an aging trajectory prediction error is 2.02% with 50 cycles of 14 NCM cells. The aging trajectory prediction error is 2.68% with five cycles of 123 LFP cells data. The KP prediction results show that incorporating physical information regarding the aging mechanisms can improve ML prediction accuracy for small data sets. In comparison, traditional ML methods can work well on large data sets without physics information.

The high accuracy of PGML-DTR with fewer training samples is attributed to four aspects. 1) the mechanism features can reflect the aging mechanism inside the battery. 2) the accelerated aging battery MFs with weak correlations are caused by complex feature sub-relationships and aging mechanisms. 3) the relationship of MFs with weak correlations can be divided into two sub-relationships corresponding to two physical regions. These two sub-relations can be well-trained for two independent DTRs. 4) the DTR model has good regression and prediction ability for complex nonlinear systems. The DTR can have good prediction accuracy in more training samples when the features are weakly correlated and the physics information is insufficient.

It highlights the prospects of combining physics information, domain knowledge, and ML for analyzing and predicting complex nonlinear systems, such as Li-ion batteries.

APPENDIX

The accelerated aging features of Cell z are extracted from the evolution of the discharge curve, the IC curve, and the DV curve from the r th cycle (i.e., the reference cycle) to the n th cycle. The steps of feature extraction are given below.

Step 1: Extract the discharge capacity versus voltage curve and discharge time versus voltage curve of Cell z in the voltage boundary range of 2.9 V to 4 V during the discharge process of the n th cycle, denoted as $Q_n^z(V_i)$ and $t_n^z(V_i)$, respectively. Then, calculate the changes of discharge capacity and discharge time during a fixed voltage and time interval. Finally, obtain $dQ/dV_n^z(V_i)$ and $dV/dt_n^z(V_i)$ data, $V_i \in (2.9 \text{ V} - 4 \text{ V})$.

Step 2: Use (A.1), (A.2), and (A.3) to calculate the changes of $Q_n^z(V_i)$, $dV/dt_n^z(V_i)$, and $dQ/dV_n^z(V_i)$ of Cell z from the 15th to the n th cycles, i.e.,

$$\Delta Q_n^z(V_i) = Q_n^z(V_i) - Q_r^z(V_i) \quad (\text{A.1})$$

$$\Delta dV/dt_n^z(V_i) = dV/dt_n^z(V_i) - dV/dt_r^z(V_i) \quad (\text{A.2})$$

$$\Delta dQ/dV_n^z(V_i) = dQ/dV_n^z(V_i) - dQ/dV_r^z(V_i) \quad (\text{A.3})$$

where $V_i \in (2.9 \text{ V} - 4 \text{ V})$, $i=1, 2, \dots, l_v$ is the index of the voltage data, and l_v is the number of voltage data. $Q_n^z(V_i)$ and $Q_r^z(V_i)$ represent the relationships between discharge capacity and voltage of Cell z at the n th cycle and the reference cycle, respectively. $\Delta Q_n^z(V_i)$ is the difference between the discharge capacity versus voltage curve at the reference cycle and the n th cycle of Cell z . $dV/dt_n^z(V_i)$ is the DV curve of Cell z at the n th

cycle; $dV/dt_r^z(V_i)$ is the DV curve of Cell z at the reference cycle. $\Delta dV/dt_n^z(V_i)$ is the difference between the DV curve at the reference cycle and the n th cycle of Cell z . $dQ/dV_n^z(V_i)$ is the IC curve of Cell z at the n th cycle; $dQ/dV_r^z(V_i)$ is the IC curve of Cell z at the reference cycle. $\Delta dQ/dV_n^z(V_i)$ is the difference between the IC curve at the reference cycle and the n th cycle of Cell z .

Step 3: Extract 17 features from the curves of $\Delta Q_n^z(V_i)$, $\Delta dV/dt_n^z(V_i)$, and $\Delta dQ/dV_n^z(V_i)$. The mean values of these three curves are calculated by (A.4)–(A.6), with which 17 statistical features are calculated by (A.7)–(A.23).

$$\overline{\Delta Q_n^z} = \frac{1}{k} \sum_{i=1}^k \Delta Q_n^z(V_i) \quad (\text{A.4})$$

$$\overline{\Delta dV/dt_n^z} = \frac{1}{k} \sum_{i=1}^k \Delta dV/dt_n^z(V_i) \quad (\text{A.5})$$

$$\overline{\Delta dQ/dV_n^z} = \frac{1}{k} \sum_{i=1}^k \Delta dQ/dV_n^z(V_i) \quad (\text{A.6})$$

$$f_{1,n}^z = \ln(|\overline{\Delta Q_n^z}|) \quad (\text{A.7})$$

$$f_{2,n}^z = \ln(|\max(\Delta Q_n^z(V_i))|) \quad (\text{A.8})$$

$$f_{3,n}^z = \ln(|\min(\Delta Q_n^z(V_i))|) \quad (\text{A.9})$$

$$f_{4,n}^z = \ln(|\frac{1}{k-1} \sum_{i=1}^k (\Delta Q_n^z(V_i) - \overline{\Delta Q_n^z})^2|) \quad (\text{A.10})$$

$$f_{5,n}^z = \frac{\frac{1}{k} \sum_{i=1}^k (\Delta Q_n^z(V_i) - \overline{\Delta Q_n^z})^3}{\left(\sqrt{\frac{1}{k} \sum_{i=1}^k (\Delta Q_n^z(V_i) - \overline{\Delta Q_n^z})^2}\right)^3} \quad (\text{A.11})$$

$$f_{6,n}^z = \ln(|\overline{\Delta dQ/dV_n^z}|) \quad (\text{A.12})$$

$$f_{7,n}^z = \ln(|\max(\Delta dQ/dV_n^z(V_i))|) \quad (\text{A.13})$$

$$f_{8,n}^z = \ln(|\min(\Delta dQ/dV_n^z(V_i))|) \quad (\text{A.14})$$

$$f_{9,n}^z = \ln(|\frac{1}{k-1} \sum_{i=1}^k (\Delta dQ/dV_n^z(V_i) - \overline{\Delta dQ/dV_n^z})^2|) \quad (\text{A.15})$$

$$f_{10,n}^z = \frac{\frac{1}{k} \sum_{i=1}^k (\Delta dQ/dV_n^z(V_i) - \overline{\Delta dQ/dV_n^z})^3}{\left(\sqrt{\frac{1}{k} \sum_{i=1}^k (\Delta dQ/dV_n^z(V_i) - \overline{\Delta dQ/dV_n^z})^2}\right)^3} \quad (\text{A.16})$$

$$f_{11,n}^z = \ln(|\overline{\Delta dV/dt_n^z}|) \quad (\text{A.17})$$

$$f_{12,n}^z = \ln(|\max(\Delta dV/dt_n^z(V_i))|) \quad (\text{A.18})$$

$$f_{13,n}^z = \ln(|\min(\Delta dV/dt_n^z(V_i))|) \quad (\text{A.19})$$

$$f_{14,n}^z = \ln(|\frac{1}{k-1} \sum_{i=1}^k (\Delta dV/dt_n^z(V_i) - \overline{\Delta dV/dt_n^z})^2|) \quad (\text{A.20})$$

$$f_{15,n}^z = \frac{\frac{1}{k} \sum_{i=1}^k (\Delta dV/dt_n^z(V_i) - \overline{\Delta dV/dt_n^z})^3}{\left(\sqrt{\frac{1}{k} \sum_{i=1}^k (\Delta dV/dt_n^z(V_i) - \overline{\Delta dV/dt_n^z})^2}\right)^3} \quad (\text{A.21})$$

$$f_{16,n}^z = t_n^z - t_r^z \quad (\text{A.22})$$

$$f_{17,n}^z = Q_{\text{dis},n}^z - Q_{\text{dis},r}^z \quad (\text{A.23})$$

where $Q_{\text{dis},n}^z$ and $Q_{\text{dis},r}^z$ are the total discharge capacity of the n th cycle and the reference cycle, respectively. As mentioned earlier, the features are extracted within the voltage boundary

range of 2.9 V–4 V for the NCM cells. For the LFP cells, the features are extracted from the voltage range of 2.02 V–3.58 V. In [19], the influence of the selection of the reference cycle on the prediction accuracy during the feature extraction was analyzed on the LFP dataset. It was found that when the reference cycle is earlier than 20, and the cycle number for feature extraction is greater than 50, the changes of the discharge, IC, and DV curves can be used to predict the aging trajectory with high accuracy. Hence, we adopted $r = 15$ in this work as the reference cycle as an example. On the other hand, for the LFP dataset, since the features are extracted before five cycles, we use $r = 2$ as the reference cycle.

REFERENCES

- [1] X. Hu, H. Yuan, C. Zou, Z. Li, and L. Zhang, "Co-estimation of state of charge and state of health for lithium-ion batteries based on fractional-order calculus," *IEEE Trans. Veh. Technol.*, vol. 67, no. 11, pp. 10319-10329, 2018.
- [2] L. Su, M. Wu, Z. Li, and J. Zhang, "Cycle life prediction of lithium-ion batteries based on data-driven methods," *eTransport.*, vol. 10, p. 100137, 2021.
- [3] X. Li, C. Yuan, Z. Wang, J. He, and S. Yu, "Lithium battery state-of-health estimation and remaining useful lifetime prediction based on non-parametric aging model and particle filter algorithm," *eTransport.*, vol. 11, p. 100156, 2022.
- [4] Y. Yang, "A machine-learning prediction method of lithium-ion battery life based on charge process for different applications," *Appl. Energy*, vol. 292, p. 116897, 2021.
- [5] X. Hu, Y. Che, X. Lin, and S. Onori, "Battery health prediction using fusion-based feature selection and machine learning," *IEEE Trans. Transport. Electricif.*, vol. 7, no. 2, pp. 382-398, 2021.
- [6] X. Tang, K. Liu, X. Wang, F. Gao, J. Marco, and W. D. Widanage, "Model migration neural network for predicting battery aging trajectories," *IEEE Trans. Transport. Electricif.*, vol. 6, no. 2, pp. 363-374, 2020.
- [7] C. She, Y. Li, C. Zou, T. Wik, Z. Wang, and F. Sun, "Offline and online blended machine learning for lithium-ion battery health state estimation," *IEEE Trans. Transport. Electricif.*, vol. 8, no. 2, pp. 1604-1618, Aug. 2022.
- [8] Z. Wei, H. Ruan, Y. Li, J. Li, C. Zhang, and H. He, "Multistage state of health estimation of lithium-ion battery with high tolerance to heavily partial charging," *IEEE Trans. Power Electron.*, vol. 37, no. 6, pp. 7432-7442, Jun. 2022.
- [9] K. Liu, X. Hu, Z. Wei, Y. Li, and Y. Jiang, "Modified Gaussian process regression models for cyclic capacity prediction of lithium-ion batteries," *IEEE Trans. Transport. Electricif.*, vol. 5, no. 4, pp. 1225-1236, 2019.
- [10] T. Hu, H. Ma, H. Sun, and K. Liu, "Electrochemical-theory-guided modeling of the conditional generative adversarial network for battery calendar aging forecast," *IEEE J. Emerg. Sel. Topics Power Electron.*, vol. 11, no. 1, pp. 67-77, 2023.
- [11] X. Han, L. Lu, Y. Zheng, X. Feng, Z. Li, J. Li, and M. Ouyang, "A review on the key issues of the lithium ion battery degradation among the whole life cycle," *eTransport.*, vol. 1, p. 100005, 2019.
- [12] X. Hu, J. Jiang, D. Cao, and B. Egardt, "Battery health prognosis for electric vehicles using sample entropy and sparse Bayesian predictive modeling," *IEEE Trans. Ind. Electron.*, vol. 63, no. 4, pp. 2645-2656, Apr. 2016.
- [13] A. Nuhic, T. Terzimehic, T. Soczka-Guth, M. Buchholz, and K. Dietmayer, "Health diagnosis and remaining useful life prognostics of lithium-ion batteries using data-driven methods," *J. Power Sources*, vol. 239, pp. 680-688, 2013.
- [14] Y. Li, C. Zou, M. Berecibar, E. Nanini-Maury, J. C.-W. Chan, P. van den Bossche, et al., "Random forest regression for online capacity estimation of lithium-ion batteries," *Appl. Energy*, vol. 232, pp. 197-210, 2018.
- [15] Y. Zhang, R. Xiong, H. He, and M. G. Pecht, "Long short-term memory recurrent neural network for remaining useful life prediction of lithium-ion batteries," *IEEE Trans. Veh. Technol.*, vol. 67, no. 7, pp. 5695-5705, 2018.
- [16] S. Saxena, L. Ward, J. Kubal, W. Lu, S. Babinec, and N. Paulson, "A convolutional neural network model for battery capacity fade curve prediction using early life data," *J. Power Sources*, vol. 542, p. 231736, 2022.
- [17] D. Chen, W. Zhang, C. Zhang, B. Sun, X. Cong, S. Wei, and J. Jiang, "A novel deep learning-based life prediction method for lithium-ion batteries with strong generalization capability under multiple cycle profiles," *Appl. Energy*, vol. 327, p. 120114, 2022.
- [18] Y. Wei and D. Wu, "Prediction of state of health and remaining useful life of lithium-ion battery using graph convolutional network with dual attention mechanisms," *Rel. Eng. Syst. Safety*, vol. 230, p. 108947, 2023.
- [19] K. A. Severson, P. M. Attia, N. Jin, N. Perkins, B. Jiang, Z. Yang, et al., "Data-driven prediction of battery cycle life before capacity degradation," *Nat. Energy*, vol. 4, no. 5, pp. 383-391, 2019.
- [20] S. Greenbank and D. Howey, "Automated feature extraction and selection for data-driven models of rapid battery capacity fade and end of life," *IEEE Trans. Ind. Inform.*, vol. 18, no. 5, pp. 2965-2973, 2022.
- [21] C. Zhang, Y. Wang, Y. Gao, F. Wang, B. Mu, and W. Zhang, "Accelerated fading recognition for lithium-ion batteries with nickel-cobalt-manganese cathode using quantile regression method," *Appl. Energy*, vol. 256, p. 113841, 2019.
- [22] Y. Gao, S. Yang, J. Jiang, C. Zhang, W. Zhang, and X. Zhou, "The mechanism and characterization of accelerated capacity deterioration for lithium-ion battery with $\text{Li}(\text{NiMnCo})\text{O}_2$ cathode," *J. Electrochem. Soc.*, vol. 166, no. 8, pp. A1623-A1635, 2019.
- [23] S. Saxena, Y. Xing, D. Kwon, and M. Pecht, "Accelerated degradation model for C-rate loading of lithium-ion batteries," *Int. J. Electr. Power Energy Syst.*, vol. 107, pp. 438-445, 2019.
- [24] L. Lu, X. Han, J. Li, J. Hua, and M. Ouyang, "A review on the key issues for lithium-ion battery management in electric vehicles," *J. Power Sources*, vol. 226, pp. 272-288, 2013.
- [25] K. Liu, X. Tang, R. Teodorescu, F. Gao, and J. Meng, "Future ageing trajectory prediction for lithium-ion battery considering the knee point effect," *IEEE Trans. Energy Convers.*, vol. 37, no. 2, pp. 1282-1291, 2022.
- [26] K. Liu, Q. Peng, R. Teodorescu, and A. M. Foley, "Knowledge-guided data-driven model with transfer concept for battery calendar ageing trajectory Prediction," *IEEE/CAA J. Autom. Sinica*, vol. 10, no. 1, pp. 272-274, 2023.
- [27] S. J. Pan and Q. Yang, "A survey on transfer learning," *IEEE Trans. Knowl. Data Eng.*, vol. 22, no. 10, pp. 1345-1359, 2010.
- [28] Z. Cao, K. You, M. Long, J. Wang, and Q. Yang, "Learning to transfer examples for partial domain adaptation," in *Proc. IEEE/CVF Conf. Comput. Vision Pattern Recognit. (CVPR) 15-20 Jun. 2019*, pp. 2980-2989.
- [29] J. Zhu, Y. Wang, Y. Huang, R. B. Gopaluni, Y. Cao, M. Heere, et al., "Data-driven capacity estimation of commercial lithium-ion batteries from voltage relaxation," *Nat. Commun.*, vol. 13, no. 1, 2022.
- [30] J. Ma, P. Shang, X. Zou, N. Ma, Y. Ding, J. Sun, et al., "A hybrid transfer learning scheme for remaining useful life prediction and cycle life test optimization of different formulation Li-ion power batteries," *Appl. Energy*, vol. 282, 2021.
- [31] Y. Tan and G. Zhao, "Transfer learning with long short-term memory network for state-of-health prediction of lithium-ion batteries," *IEEE Trans. Ind. Electron.*, vol. 67, no. 10, pp. 8723-8731, 2020.
- [32] Z. Deng, X. Lin, J. Cai, and X. Hu, "Battery health estimation with degradation pattern recognition and transfer learning," *J. Power Sources*, vol. 525, p. 231027, 2022.
- [33] X. Jia, C. Zhang, L. Wang, L. Zhang, and X. Zhou, "Early diagnosis of accelerated ageing for lithium-ion batteries with an integrated framework of ageing mechanisms and data-driven methods," *IEEE Trans. Transport. Electricif.*, vol. 8, no. 4, pp. 4722-4742, Dec. 2022.
- [34] X. Bian, Z. Wei, W. Li, J. Pou, D. U. Sauer, and L. Liu, "State-of-health estimation of lithium-ion batteries by fusing an open circuit voltage model and incremental capacity analysis," *IEEE Trans. Power Electron.*, vol. 37, no. 2, pp. 2226-2236, 2022.
- [35] X. Han, M. Ouyang, L. Lu, J. Li, Y. Zhang, and Z. Li, "A comparative study of commercial lithium ion battery cycle life in electrical vehicle:

- Aging mechanism identification," *J. Power Sources*, vol. 251, pp. 38-54, 2014.
- [36] Y. Gao, J. Jiang, C. Zhang, W. Zhang, and Y. Jiang, "Aging mechanisms under different state-of-charge ranges and the multi-indicators system of state-of-health for lithium-ion battery with Li(NiMnCo)O₂ cathode," *J. Power Sources*, vol. 400, pp. 641-651, 2018.
- [37] B. Vortmann-Westhoven, M. Winter, and S. Nowak, "Where is the lithium? Quantitative determination of the lithium distribution in lithium ion battery cells: Investigations on the influence of the temperature, the C-rate and the cell type," *J. Power Sources*, vol. 346, pp. 63-70, 2017.
- [38] M. Petzl, M. Kasper, and M. A. Danzer, "Lithium plating in a commercial lithium-ion battery – A low-temperature aging study," *J. Power Sources*, vol. 275, pp. 799-807, 2015.
- [39] Y.-J. Lee, H.-Y. Choi, C.-W. Ha, J.-H. Yu, M.-J. Hwang, C.-H. Doh, and J.-H. Choi, "Cycle life modeling and the capacity fading mechanisms in a graphite/LiNi_{0.6}Co_{0.2}Mn_{0.2}O₂ cell," *J. Appl. Electrochem.*, vol. 45, no. 5, pp. 419-426, 2015.
- [40] K. M. Shaju, G. V. Subba Rao, and B. V. R. Chowdari, "Performance of layered Li(Ni_{1/3}Co_{1/3}Mn_{1/3})O₂ as cathode for Li-ion batteries," *Electrochim. Acta*, vol. 48, no. 2, pp. 145-151, 2002.
- [41] C. Lin, A. Tang, H. Mu, W. Wang, and C. Wang, "Aging mechanisms of electrode materials in lithium-ion batteries for electric vehicles," *J. Chem.-NY*, vol. 2015, Art no. 104673, 2015.
- [42] D. Aurbach, "Review of selected electrode – solution interactions which determine the performance of Li and Li ion batteries," *J. Power Sources*, vol. 89, no. 2, pp. 206-218, 2000.
- [43] M. Koltypin, Y. S. Cohen, B. Markovsky, Y. Cohen, and D. Aurbach, "The study of lithium insertion – deinsertion processes into composite graphite electrodes by in situ atomic force microscopy (AFM)," *Electrochim. Commun.*, vol. 4, no. 1, pp. 17-23, 2002.
- [44] S. Ko, Y. Yamada, and A. Yamada, "An overlooked issue for high-voltage Li-ion batteries: Suppressing the intercalation of anions into conductive carbon," *Joule*, vol. 5, no. 4, pp. 998-1009, 2021.
- [45] F. Mocera, A. Soma, and D. Clerici, "Study of aging mechanisms in lithium-ion batteries for working vehicle applications," in *Proc. Int. Conf. Ecolog. Veh. Renew. Energies (EVER)*, 10-12 Sep. 2020, pp. 1-8.
- [46] T. Rauhala, K. Jalkanen, T. Romann, E. Lust, N. Omar, and T. Kallio, "Low-temperature aging mechanisms of commercial graphite/LiFePO₄ cells cycled with a simulated electric vehicle load profile—A post-mortem study," *J. Energy Storage*, vol. 20, pp. 344-356, 2018.
- [47] L. Zhang, J. Liu, L. Du, P. Fan, X. Xu, Y. Ma, P. Zuo, B. Qu, G. Yin, and Q. Fu, "LiNi_{0.5}Co_{0.2}Mn_{0.3}O₂/graphite batteries storing at high temperature: Capacity fading and raveling of aging mechanisms," *J. Power Sources*, vol. 496, p. 229858, 2021.
- [48] H. Noh, S. Youn, C. S. Yoon, and Y. Sun, "Comparison of the structural and electrochemical properties of layered Li[Ni_xCo_yMn_z]O₂ (x = 1/3, 0.5, 0.6, 0.7, 0.8 and 0.85) cathode material for lithium-ion batteries," *J. Power Sources*, vol. 233, pp. 121-130, 2013.
- [49] G. Ning, B. Haran, and B. N. Popov, "Capacity fade study of lithium-ion batteries cycled at high discharge rates," *J. Power Sources*, vol. 117, no. 1-2, pp. 160-169, 2003.
- [50] A. Swetapadma and A. Yadav, "A novel decision tree regression-based fault distance estimation scheme for transmission lines," *IEEE Trans. Power Del.*, vol. 32, no. 1, pp. 234-245, 2017.
- [51] B. Charbuty and A. Abdulazeez, "Classification based on decision tree algorithm for machine learning," *J. Appl. Sci. Technol. Trends*, vol. 2, no. 01, pp. 20-28, 2021.



Xinyu Jia (Graduate Student Member, IEEE) was born in Guangxi Province, China. He received the B.Eng. degree in electrical engineering from Beijing Jiaotong University, Beijing, China, in 2016. He is a Ph.D. student at the National Active Distribution Network Technology Research Center, Beijing Jiaotong University. He conducted scientific research as a visiting researcher with the Automatic Control, Department of Electrical Engineering, Chalmers University of Technology, Gothenburg, Sweden. His research interests include battery ageing mechanism and

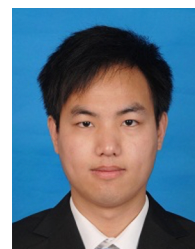
characteristics, battery life prediction, battery fault diagnosis and machine learning.



Caiping Zhang (Senior Member, IEEE) received the Ph.D. degree in vehicle engineering from the Beijing Institute of Technology in 2010. From 2010 to 2012, she was a Postdoctoral Researcher with Beijing Jiaotong University, Beijing, where she is currently a Professor with the School of Electrical Engineering. Her research interests include battery modeling, state estimation, remaining useful life prediction, fault diagnosis and warning, and smart battery management.



Yang Li (Member, IEEE) received the B.E. degree in electrical engineering from Wuhan University, Wuhan, China, in 2007, and the M.Sc. and Ph.D. degrees in power engineering from Nanyang Technological University (NTU), Singapore, in 2008 and 2015, respectively. From 2015 to 2020, he was with the Energy Research Institute, NTU, the School of Electrical Engineering and Computer Science, Queensland University of Technology, Brisbane, QLD, Australia, and the School of Automation, Wuhan University of Technology, Wuhan. Since 2020, he has been a Researcher with the Department of Electrical Engineering, Chalmers University of Technology, Gothenburg, Sweden. His research interests include modeling and control of energy storage systems in power grid and transport sectors. He serves as an Associate Editor for IEEE TRANSACTIONS ON TRANSPORTATION ELECTRIFICATION and IEEE TRANSACTIONS ON INDUSTRIAL ELECTRONICS.



Changfu Zou (Senior Member, IEEE) received the Ph.D. degree in automation and control engineering from the Department of Mechanical Engineering, University of Melbourne, VIC, Australia, in 2017. He was a Postdoctoral Researcher with the Chalmers University of Technology, Gothenburg, Sweden, where he is currently an Assistant Professor with the Automatic Control Group, Department of Electrical Engineering. His current research interests include modeling and control of energy storage systems for automotive and power grid applications. He serves as an Associate Editor for IEEE TRANSACTIONS ON TRANSPORTATION ELECTRIFICATION and for IEEE TRANSACTIONS ON VEHICULAR TECHNOLOGY.



Le Yi Wang (Life Fellow, IEEE) received the Ph.D. degree in electrical engineering from McGill University, Montreal, Canada, in 1990. Since 1990, he has been with Wayne State University, Detroit, MI, where he is currently a Professor with the Department of Electrical and Computer Engineering. His research interests include complexity and information, system identification, robust control, information processing and learning, as well as medical, automotive, communications, power systems, and computer methodologies. He was a plenary speaker at many international conferences. He serves on the IFAC Technical Committee on Modeling, Identification and Signal Processing. He was an Associate Editor of the IEEE TRANSACTIONS ON AUTOMATIC CONTROL and several other journals.



Xue Cai was born in Liaoning Province, China, in 1994. She received her Master's degree from Northeastern University. She is pursuing her Ph.D. degree at the Beijing Jiaotong University, Beijing, China. Her research interests include non-destructive diagnosis technology, electrochemical-mechanical coupling modeling, and optimal design under the external pressure of lithium-ion batteries.